Chatzaras, V., et al., 2020, Stress variations in space and time within the mantle section of an oceanic transform zone: Evidence for the seismic cycle: Geology, v. 48, https://doi.org/10.1130/G47137.1

Supplement to "Stress variations in space and time within the mantle section of an oceanic transform zone: Evidence for the seismic cycle"

Vasileios Chatzaras, Basil Tikoff, Seth C. Kruckenberg, Sarah J. Titus, Christian Teyssier, Martyn R. Drury

1. Methods

1.1 X-ray computed tomography

To determine the foliation and lineation in each peridotite sample, we estimated the spinel fabric ellipsoid using high-resolution X-ray computed tomography. Analytical work was carried out in the Department of Earth Sciences, at the University of Minnesota, Twin Cities, which houses an X5000 high-resolution micro-CT system with a twin head 225 kV cone beam X-ray source and a Dexela area detector (3073 × 3889 pixels). For a detailed description of the workflow see Chatzaras et al. (2016). We used Avizo®Fire for image processing (filtering and thresholding), separation of the mineral phase of interest (spinel), small object removal, and extracting 3D quantitative measurements. Thin sections were produced relative to the 3D spinel fabric, such that they are oriented perpendicular to the spinel-defined foliation plane, with the long axis of each thin section oriented parallel to the spinel lineation.

1.2 Electron Backscatter Diffraction

Ultrahigh polished thin sections were prepared for EBSD analysis. Thin section preparation involved polishing with diamond suspensions on 6, 3, 1 μm polishing pads, followed by 90 min of polishing with alumina slurry (0.05 μm) on a high nap pad in a vibratory polisher. Thin sections were carbon coated to reduce charging.

Microstructures were analyzed by large area (~600 mm^2) crystallographic orientation mapping of thin sections using: 1) a Tescan Mira LMU Schottky field emission scanning electron microscope (SEM) equipped with an Oxford Instruments Nordlys Max2 electron backscatter diffraction (EBSD) detector, at Boston College, and 2) a Zeiss ULTRA Plus Schottky field-emission SEM equipped with an Oxford Instruments Symmetry EBSD detector, at the University of Sydney (Australian Centre for Microscopy & Microanalysis - ACMM). Typical SEM operating conditions were 20-100 nA for beam currents and an accelerating voltage of 30 kV. Large area mapping was performed at a step size of 10 μm to ensure high density of crystallographic orientation data. High resolution mapping was performed at a 1–2 μm step size. Post-acquisition data treatment involved processing of EBSD maps using the HKL Channel5 software package. Processing included: 1) removal of isolated single pixels

differing by more than 10° from their neighbors; and 2) assignment of the average orientation of neighboring pixels to non-indexed pixels with eight nearest neighbors. The latter operation was iterated until no new pixels were filled and was repeated for non-indexed pixels with decreasing number of nearest neighbors as low as three because of the high degree of seprentinization of the analyzed samples. For grain reconstruction, a misorientation angle of 10° was used to define the lower limit of grain boundaries. Grain size analysis was performed with the HKL Channel5 software. Grain size was analyzed using the linear intercept and the equivalent circular diameter methods. For the linear intercept method, grain size was estimated from the arithmetic mean of the intercept lengths distribution and a scaling factor of 1.5 was used (Underwood, 1970). We used the open-source GrainSizeTools script (Lopez-Sanchez and Llana-Fúnez, 2015) to construct grain size distributions of the number- and area-weighted equivalent circular diameters. We determined the geometric mean from the number-weighted grain size distributions. To convert between the geometric mean of the equivalent circular diameter on a two-dimensional section and the mean grain size in three dimensions, a scaling factor of 1.2 was used (Underwood, 1970). We used the MTEX MATLAB toolbox (version 3.5) for crystallographic preferred orientation analysis. One point per grain data (i.e., mean crystallographic orientation of each grain) were calculated for the reconstructed grains and the orientations of crystallographic axes were plotted on equal area, lower-hemisphere projections.

1.3 Electron Probe Microanalysis.

The major and minor element compositions of olivine, spinel, orthopyroxene, and clinopyroxene were analyzed by wavelength-dispersion spectrometry (WDS) with a Cameca SX50 microprobe in the Department of Geoscience, at the University of Wisconsin-Madison and a JEOL JXA-8530F Hyperprobe Field Emission Electron probe microanalyser in GeoLab, at Utrecht University. Operating conditions were: 15 kV accelerating voltage, 20 nA beam current (Faraday cup), and beam diameter of 1 μm.

2. Figures

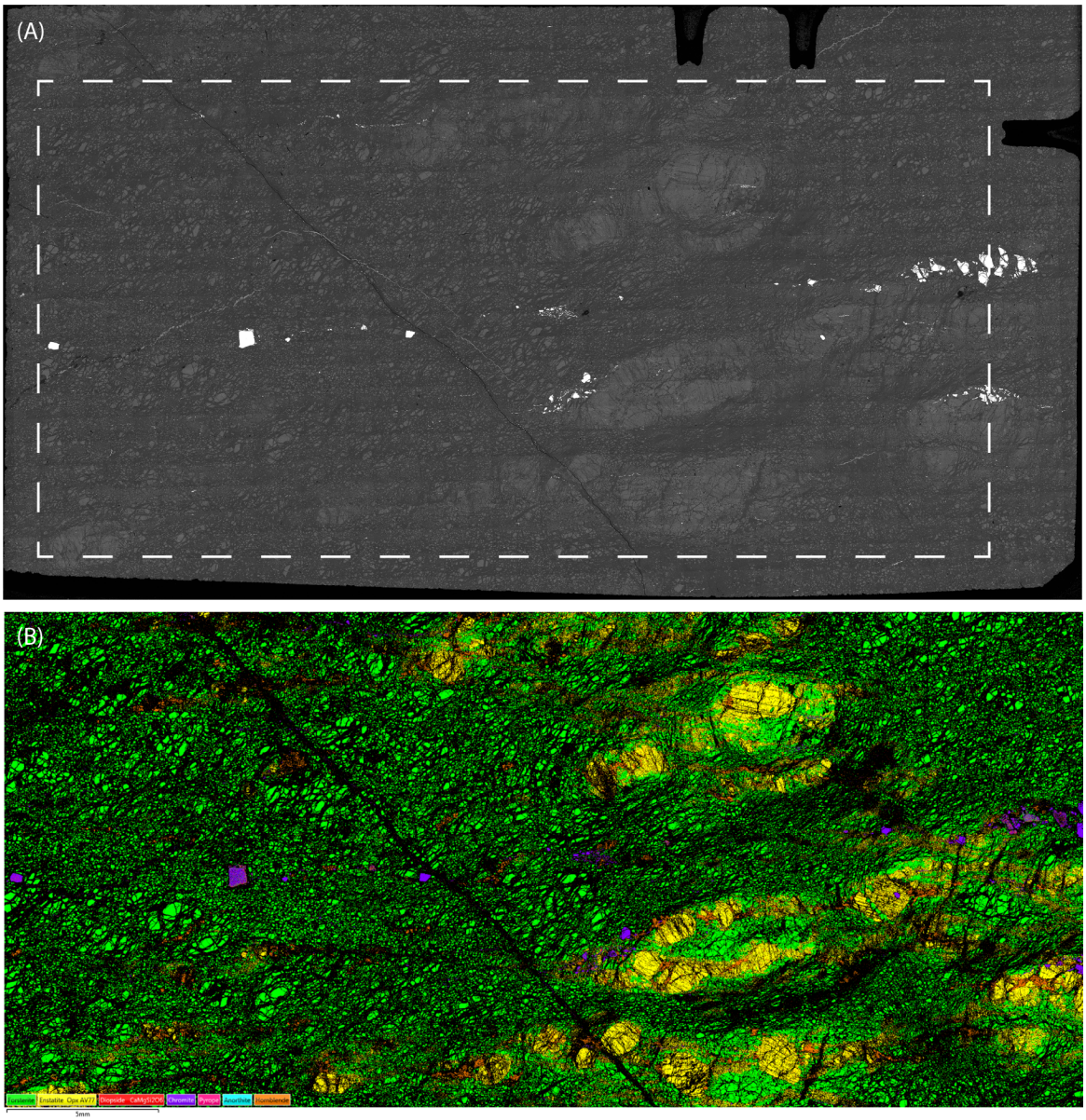

Figure DR1. Raw thin section maps of a harzburgite from the Bogota Peninsula shear zone area, produced at the Scanning Electron Microscope (SEM). A: Full thin section Backscatter electron (BSE) map. B: Raw EBSD phase map as exported from Aztec software, used for the acquisition of the EBSD data. The parallelogram in A defines the location of the EBSD map. Black areas have returned zero solution and correspond to serpentinite veins.

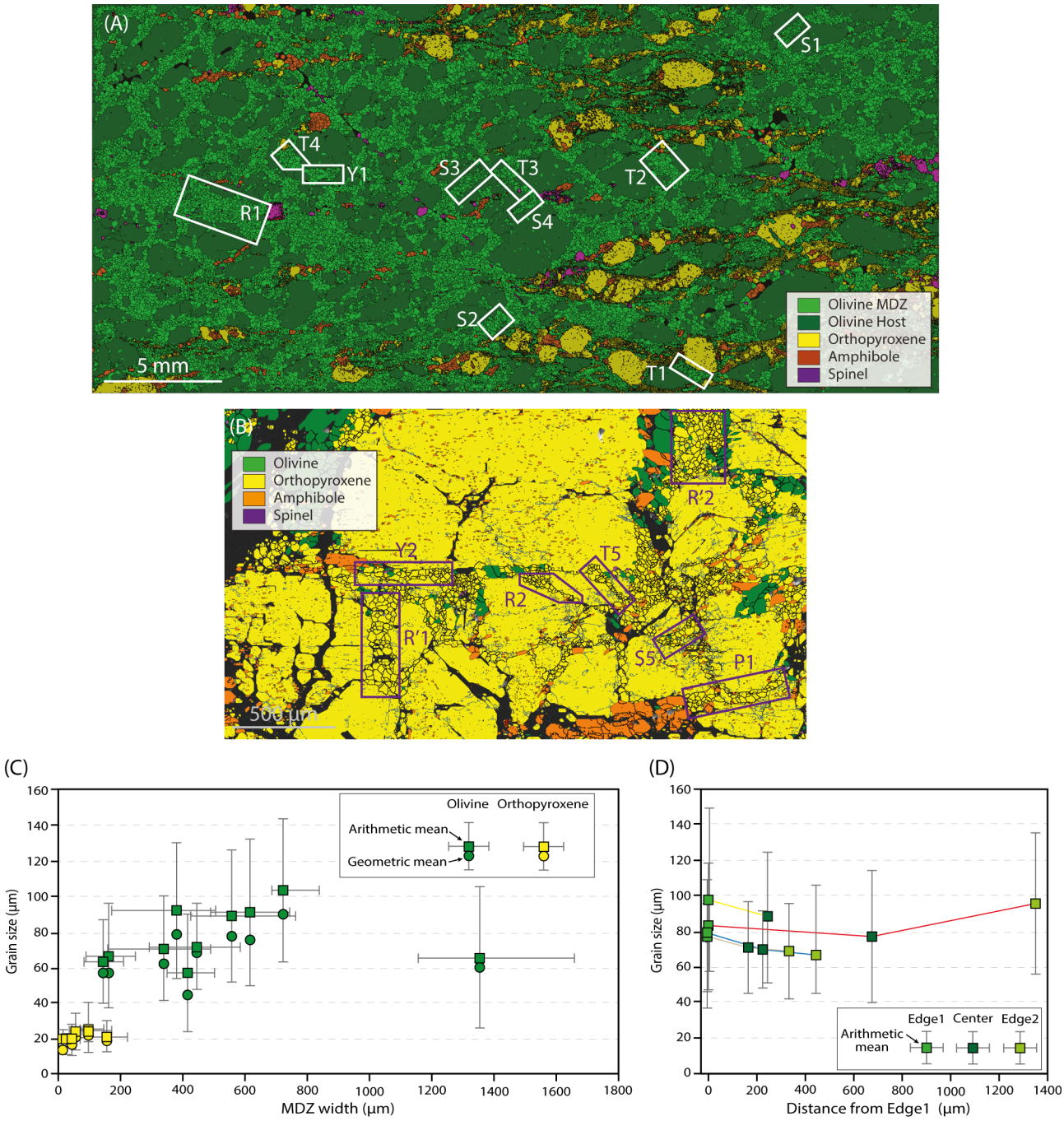

Figure DR2. Recrystallized grain size of olivine and orthopyroxene in micro-deformation zones (MDZs). A, B: EBSD phase maps from a harzburgite that hosts MDZs, which contain recrystallized olivine (A) or orthopyroxene (B). Boxes highlight the areas of the MDZs where grain size analysis was performed. C: Relationship between the size of the recrystallized grains in the MDZs and the width of the MDZs. Grain size is extracted from high-resolution EBSD maps constructed with a step size of 1–2 µm. Grain size is estimated using the equivalent circular diameter method and is plotted as the arithmetic mean and geometric mean of the grain size distribution. Standard deviation of the arithmetic mean is shown with the vertical error bars, and horizontal error bars reflect the range of the MDZs' width. Arithmetic mean is plotted on the mean MDZ width. Correlation between the grain size and the width of the MDZs is only observed for MDZs with width between 450 and 800 µm. D: Variation of grain size across the MDZs. Vertical error bars show the standard deviation of the arithmetic mean of the grain size distribution. Grain size either decreases across the MDZs or increases from the center to the edges of the MDZs. The grain size and MDZ width data used in C and D are presented in Table DR1.

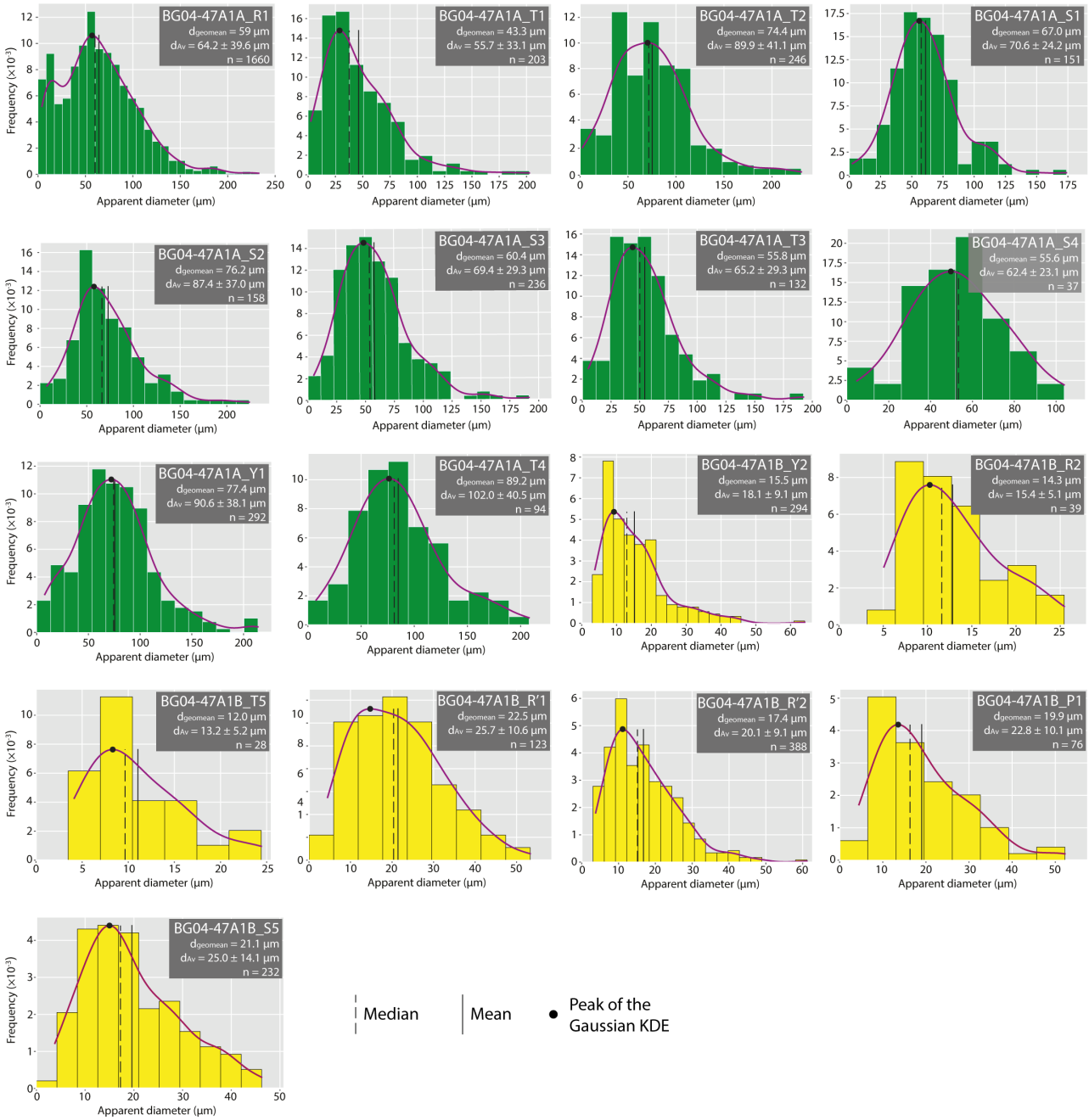

Figure DR3. Histograms of the 2D grain size distribution of recrystallized olivine and orthopyroxene in the MDZs highlighted in Figure DR2. The mean, median, and the peak of the Gaussian kernel density estimator (KDE) of each distribution are plotted in each histogram. The arithmetic mean with its standard deviation and the geometric mean is given; a scaling factor of 1.2 was used to convert 2D to 3D grain size. The grain size distributions were constructed using the open-source GrainSizeTools script (Lopez-Sanchez and Llana-Fúnez, 2015).

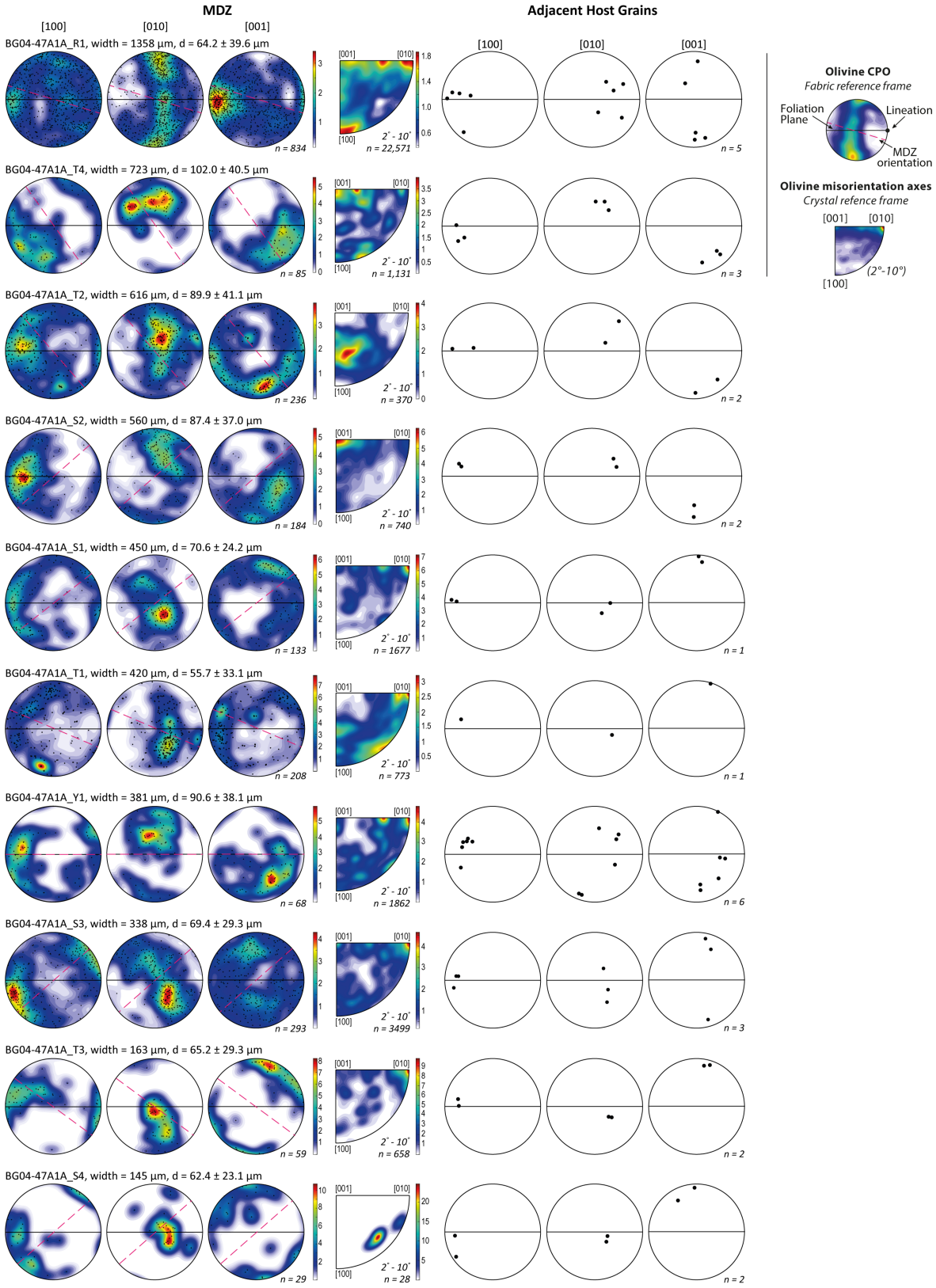

Figure DR4. Crystallographic orientations and low-angle misorientations of olivine in the MDZs and adjacent host grains. Samples are organized with decreasing of MDZ width. Crystallographic orientations are plotted as one point per grain data sets in lower hemisphere equal area projections, relative to the spinel fabric. Color scales are for multiples of uniform distribution. For each sample, the MDZ width, the average grain size, and the number of grains analyzed, are given. Misorientation axes are from correlated misorientation angles between 2° and 10°. Inverse pole figures are in the crystallographic reference frame.

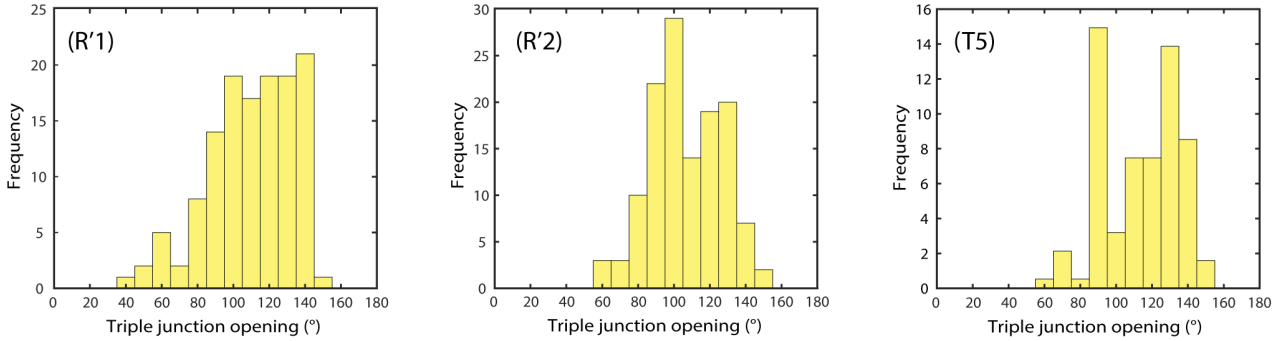

Figure DR5. Frequency distributions of the opening angles of grain triple junctions in MDZs containing orthopyroxene. Data are from the DMZs R'1, R'2, and T5 shown in Figure DR2. The number of stable (120°) triple junctions is 25%, 25%, and 11%, in R'1, R'2, and T5, respectively.

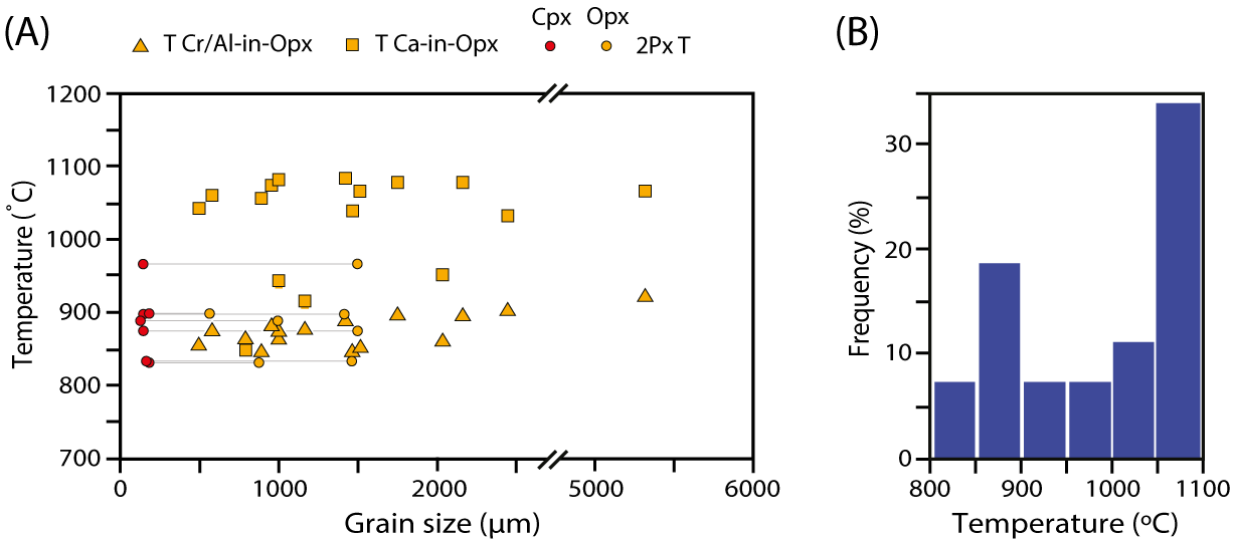

Figure DR6. Calculated equilibration temperatures in harzburgites that host micro-deformation zones. A: We applied three geothermometers based on major element mineral compositions of orthopyroxene and clinopyroxene measured with microprobe (Tables DR1 and DR2). These geothermometers include the Ca-in-Opx geothermometer (Brey and Köhler, 1990), Al/Cr-in-Opx geothermometer (Witt-Eickschen and Seck, 1991), and two-pyroxenes geothermometer (Taylor, 1998). For pressure-dependent thermometers temperatures were calculated at an assumed pressure of 700 MPa. The effect of pressure on calculated two-pyroxene temperatures is 0.02 °C/MPa. The horizontal lines link the orthopyroxene and clinopyroxene grain sizes in the case of the two-pyroxene thermometer. Opx: orthopyroxene; Cpx: clinopyroxene. B: Frequency diagram of the equilibration temperatures calculated with the three geothermometers for the harzburgites in the Bogota Peninsula shear zone.

3. Tables

Table DR1. Grain size of olivine and orthopyroxene in the micro-deformation zones highlighted in Figures DR2A and DR2B. The grain size data are summarized in Figures DR2C and DR2D of the Supplementary Material.

	Sample	MDZ	Composition	MDZ width			MDZ grain size				
				Mean (µm)	Minimum (µm)	Maximum (µm)	$d_{Av} \pm SD$ (µm)	$d_{Geomean}$ (µm)	$d_{Av\ Edge1} \pm SD$ (µm)	$d_{Av\ Center} \pm SD$ (µm)	$d_{Av\ Edge1} \pm SD$ (µm)
1	BG04-47A1A	R1	Olivine	1358	1146	1653	64.2 ± 39.6	59.0	82.1 ± 35.8	75.7 ± 37.1	94.5 ± 39.5
2	BG04-47A1A	T1	Olivine	420	343	495	55.7 ± 33.1	43.3	—	—	—
3	BG04-47A1A	T2	Olivine	616	481	734	89.9 ± 41.1	74.4	—	—	—
4	BG04-47A1A	S1	Olivine	450	285	579	70.6 ± 24.2	67.0	75.6 ± 19.5	69.2 ± 21.9	65.8 ± 21.2
5	BG04-47A1A	S2	Olivine	560	418	753	87.4 ± 37.0	76.2	78.0 ± 30.3	70.1 ± 26.0	67.6 ± 26.9
6	BG04-47A1A	S3	Olivine	338	148	480	69.4 ± 29.3	60.4	—	—	—
7	BG04-47A1A	T3	Olivine	163	82	237	65.2 ± 29.3	55.8	—	—	—
8	BG04-47A1A	S4	Olivine	145	73	199	62.4 ± 23.1	55.6	—	—	—
9	BG04-47A1A	Y1	Olivine	381	160	496	90.6 ± 38.1	77.4	—	—	—
10	BG04-47A1A	T4	Olivine	723	675	833	102.0 ± 40.5	89.2	—	—	—
11	BG04-47A1B	Y2	Orthopyroxene	43	17	62	18.1 ± 9.1	15.5	—	—	—
12	BG04-47A1B	R2	Orthopyroxene	30	17	47	15.4 ± 5.1	14.3	—	—	—
13	BG04-47A1B	T5	Orthopyroxene	17	11	27	13.2 ± 5.2	12.0	—	—	—
14	BG04-47A1B	R'1	Orthopyroxene	101	65	164	25.7 ± 10.6	22.5	—	—	—
15	BG04-47A1B	R'2	Orthopyroxene	160	87	216	20.1 ± 9.1	17.4	96.7 ± 51.6	87.3 ± 36.6	—
16	BG04-47A1B	P1	Orthopyroxene	57	26	99	22.8 ± 10.1	19.9	—	—	—
17	BG04-47A1B	S5	Orthopyroxene	98	52	136	25.0 ± 14.1	21.1	—	—	—

MDZ: Micro-Deformation Zone; d: grain size; Av: Arithmetic mean; Geomean: Geometric mean; SD: Standard deviation; grain size is estimated using the equivalent circular diameter method and is reported with its corrected value, using a correction factor of 1.2.

Table DR2. Major-element compositions and grain size of orthopyroxene grains

Sample	**KA04-24A1**	**KA04-24A1**	**KA04-24A1**	**KA04-24A1**	**KA04-24A1**	**KA04-24A1**	**KA04-24A1**	**KA04-24A1**	**KA04-24A1**	**KA04-24A1**
Opx grain	Opx1	Opx2	Opx3	Opx4	Opx5	Opx15	Opx16a	Opx17	Opx18	Opx27a
wt. %										
SiO_2	57.28	57.61	57.51	57.47	57.28	57.41	57.63	57.62	57.41	57.55
TiO_2	0.00	0.02	0.00	0.01	0.00	0.01	0.01	0.00	0.01	0.01
Al_2O_3	1.40	1.22	1.22	1.20	1.28	1.31	1.24	1.20	1.29	1.36
Cr_2O_3	0.61	0.58	0.49	0.43	0.51	0.53	0.47	0.45	0.50	0.55
FeO	5.52	5.56	5.52	5.64	5.67	5.54	5.62	5.57	5.65	5.53
MnO	0.13	0.12	0.14	0.14	0.14	0.14	0.14	0.14	0.14	0.12
MgO	33.17	33.47	33.51	33.57	33.26	33.10	33.28	33.43	33.37	33.21
CaO	1.23	1.07	1.10	1.19	1.27	1.29	1.29	1.13	1.21	1.29
Na_2O	0.01	0.01	0.00	0.00	0.00	0.01	0.00	0.01	0.00	0.00
Sum	99.36	99.64	99.50	99.65	99.42	99.44	99.67	99.55	99.58	99.63
Cations per 6 oxygen atoms										
Si	1.984	1.988	1.987	1.985	1.984	1.986	1.989	1.990	1.984	1.987
Ti	0.000	0.000	0.000	0.000	0.000	0.000	0.000	0.000	0.000	0.000
Al	0.057	0.050	0.050	0.049	0.052	0.054	0.50	0.049	0.052	0.055
Cr	0.017	0.016	0.013	0.012	0.014	0.015	0.013	0.012	0.014	0.015
Fe	0.160	0.160	0.160	0.163	0.164	0.160	0.162	0.161	0.163	0.160
Mn	0.004	0.003	0.004	0.004	0.004	0.004	0.004	0.004	0.004	0.004
Mg	1.712	1.722	1.726	1.728	1.717	1.712	1.712	1.721	1.720	1.709
Ca	0.046	0.039	0.041	0.044	0.047	0.048	0.048	0.042	0.045	0.048
Na	0.000	0.001	0.000	0.000	0.000	0.000	0.000	0.001	0.000	0.000
Sum	3.980	3.979	3.981	3.985	3.983	3.980	3.979	3.980	3.982	3.978
Grain size (μm)	5328	2454	1475	893	962	1431	1007	507	584	1760

Table DR2 (cont.). Major-element compositions and grain size of orthopyroxene grains

Sample	KA04-24A1	KA04-24A1	TH04-6B1	TH04-6B1	TH04-6B1	TH04-6B1
Opx grain	Opx28a	Opx29	Opx16b	Opx26	Opx27b	Opx28b
wt. %						
SiO_2	57.74	57.66	56.44	56.56	56.50	56.49
TiO_2	0.01	0.00	0.01	0.00	0.01	0.01
Al_2O_3	1.35	1.27	1.30	1.25	1.23	1.25
Cr_2O_3	0.55	0.47	0.47	0.51	0.50	0.47
FeO	5.52	5.70	5.56	5.37	5.28	5.21
MnO	0.15	0.15	0.13	0.07	0.13	0.14
MgO	33.24	33.38	33.35	33.35	34.92	35.01
CaO	1.29	1.21	0.49	0.67	0.75	0.08
Na_2O	0.00	0.01	0.01	0.01	0.01	0.01
Sum	99.84	99.85	99.64	99.79	99.32	99.44
Cations per 6 oxygen atoms						
Si	1.989	1.987	1.952	1.951	1.958	1.956
Ti	0.000	0.000	0.000	0.000	0.000	0.000
Al	0.055	0.052	0.053	0.051	0.050	0.051
Cr	0.015	0.013	0.013	0.014	0.014	0.013
Fe	0.159	0.164	0.151	0.155	0.153	0.151
Mn	0.004	0.004	0.004	0.002	0.004	0.004
Mg	1.707	1.715	1.823	1.818	1.804	1.807
Ca	0.048	0.045	0.018	0.025	0.028	0.030
Na	0.000	0.000	0.001	0.000	0.001	0.001
Sum	3.976	3.981	4.015	4.016	4.011	4.012
Grain size (μm)	2166	1516	793	1171	1005	2040

Table DR3. Major-element compositions and grain size of clinopyroxene grains

Sample	KA04-24A1	KA04-24A1	KA04-24A1	KA04-24A1	KA04-24A1	KA04-24A1	KA04-24A1
Opx grain	Cpx6	Cpx7	Cpx12	Cpx13	Cpx14	Cpx25	Cpx26
wt. %							
SiO_2	54.68	54.39	54.71	54.96	54.82	54.87	55.04
TiO_2	0.01	0.03	0.01	0.02	0.02	0.01	0.01
Al_2O_3	1.37	1.54	1.39	1.41	1.42	1.46	1.56
Cr_2O_3	0.66	0.80	0.64	0.70	0.71	0.75	0.76
FeO	2.07	2.15	2.18	2.29	2.26	2.17	2.40
MnO	0.07	0.05	0.07	0.06	0.09	0.08	0.08
MgO	17.48	17.24	17.60	17.60	17.37	17.27	17.69
CaO	23.74	23.66	23.33	23.17	23.40	23.49	22.77
Na_2O	0.19	0.18	0.16	0.15	0.18	0.19	0.15
Sum	100.28	100.05	100.10	100.37	100.27	100.30	100.48
Cations per 6 oxygen atoms							
Si	1.976	1.971	1.978	1.981	1.980	1.981	1.980
Ti	0.000	0.001	0.000	0.001	0.001	0.000	0.000
Al	0.058	0.066	0.059	0.060	0.060	0.062	0.066
Cr	0.019	0.023	0.018	0.020	0.020	0.021	0.022
Fe	0.062	0.065	0.066	0.069	0.068	0.066	0.072
Mn	0.002	0.002	0.002	0.020	0.003	0.003	0.002
Mg	0.942	0.932	0.949	0.946	0.935	0.929	0.949
Ca	0.919	0.919	0.904	0.895	0.905	0.909	0.878
Na	0.013	0.012	0.011	0.011	0.012	0.013	0.011
Sum	3.992	3.990	3.988	3.984	3.985	3.984	3.981
Grain size (μm)	191	2454	198	156	143	161	161

Table DR4. Equilibration temperature data estimated based on major element compositions and geothermometers. The temperature data are summarized in Figure DR1.

Geothermometer	$T_{Ca\text{-}Opx}$	$T_{Al/Cr\text{-}Opx}$	T_T
Opx1	1069	923	—
Opx2	1031	902	—
Opx3	1040	716	—
Opx4	1060	846	—
Opx5	1078	881	—
Opx15	1082	890	—
Opx16a	1081	863	—
Opx17	1046	856	—
Opx18	1064	876	—
Opx27a	1082	898	—
Opx28a	1082	895	—
Opx29	1064	863	—
Opx3-Cpx7	—	—	837
Opx4-Cpx6	—	—	835
Opx15-Cpx12	—	—	898
Opx16a-Cpx14	—	—	886
Opx18-Cpx12	—	—	897
Opx29-Cpx25	—	—	873
Opx29-Cpx26	—	—	965
Opx16b	857	863	—
Opx26	918	877	—
Opx27b	945	873	—
Opx28b	951	862	—

Phase numbers refer to the numbers shown in Tables DR1 and DR2. The temperature data are summarized in Figure DR1. $T_{Ca\text{-}Opx}$ from Brey and Köhler (1990); $T_{Cr/Al\text{-}Opx}$ from Witt-Eickschen and Seck (1991); T_T from Taylor (1998); For pressure-dependent geothermometers, temperatures are estimated at a pressure of 700 MPa.

Table DR5. Grain size of olivine and calculated differential stress in the Bogota Peninsula shear zone peridotites. The grain size and stress data are summarized in Figure 1b of the manuscript.

	UTM coordinate		Sample	Microstructure	Distance (km)	Host harzburgite				Micro-deformation zones			
	Easting	Northing				d_{ECD} (μm)	d_{LI} (μm)	σ_{ECD} (MPa)	σ_{LI} (MPa)	d_{ECD} (μm)	d_{LI} (μm)	σ_{ECD} (MPa)	σ_{LI} (MPa)
1	578442.27	7644629.77	KA04-06A1	Protomylonite	0.00	667.68	579.98	10.39	11.54	228.82	225.15	23.22	23.50
2	585057.57	7638796.64	KA04-21B1	Coarse granular	6.61	667.70	596.90	10.39	11.29	249.20	243.41	21.78	22.17
3	586272.69	7637845.71	KA04-22A1	Protomylonite	7.82	404.36	531.53	15.13	12.32	—	—	—	—
4	589670.80	7636060.03	KA04-18B1A	Protomylonite	11.21	653.48	552.18	10.55	11.97	171.56	170.625	28.83	28.95
5	589670.80	7636060.03	KA04-18B1B	Protomylonite	11.21	609.31	438.77	11.12	14.23	169.14	168.99	29.14	29.16
6	591113.19	7635358.36	KA04-17A	Mylonite	12.65	529.70	272.34	12.35	20.37	87.08	91.95	48.01	46.09
7	593871.58	7634567.86	KA04-24A1	Protomylonite	15.41	673.39	503.30	10.31	12.84	178.57	176.91	27.98	28.18
8	595809.59	7631527.29	KA04-25B1	Protomylonite	17.35	673.39	554.18	10.31	11.94	185.21	187.17	27.22	27.01
9	598885.25	7631348.37	BG04-54A1A	Protomylonite	20.42	404.36	529.71	15.13	12.35	—	—	—	—
10	602862.46	7630187.85	BG04-13A1B	Coarse granular	24.39	493.90	471.05	13.02	13.49	—	—	—	—
11	603075.06	7629254.20	BG04-14B1	Coarse granular	24.60	585.42	835.53	11.46	8.77	—	—	—	—
12	604303.52	7628766.68	BG04-15B1	Protomylonite	26.04	455.92	673.83	13.83	10.31	—	—	—	—
13	605815.52	7627643.66	BG04-2A1	Mylonite	27.55	420.86	549.81	14.69	12.01	—	—	—	—
14	606566.51	7626933.79	BG02-5B1	Protomylonite	28.30	383.02	525.81	15.76	12.42	—	—	—	—
15	606665.44	7626773.36	BG02-4B1A	Protomylonite	28.40	396.36	370.47	15.36	16.16	—	—	—	—
16	607324.81	7626715.51	BG02-7A1A	Mylonite	29.06	373.27	437.03	16.07	14.27	—	—	—	—
17	607324.81	7626715.51	BG02-7A1B	Mylonite	29.06	384.65	455.51	15.71	13.84	—	—	—	—
18	607734.38	7625974.81	BG02-8B1A	Mylonite	29.47	265.69	307.65	20.75	18.59	—	—	—	—
19	607734.38	7625974.81	BG02-8B1B	Mylonite	29.47	250.21	282.62	21.71	19.81	—	—	—	—
20	608205.67	7626205.98	BG02-16A1	Mylonite	29.94	247.73	337.25	21.87	17.35	—	—	—	—
21	608294.21	7626273.66	BG02-15B1A	Mylonite	30.03	321.29	402.71	17.99	15.18	—	—	—	—
22	608294.21	7626273.66	BG02-15B1B	Mylonite	30.03	321.29	282.62	17.99	19.81	—	—	—	—
23	608630.44	7626193.92	BG02-13B1	Mylonite	30.37	305.62	356.58	18.68	16.63	—	—	—	—
24	608657.68	7624845.27	BG04-8.5-1	Mylonite	30.40	282.12	353.18	19.84	16.75	—	—	—	—
25	609103.24	7625875.26	BG02-12B1	Mylonite	30.85	438.05	564.44	14.25	11.78	—	—	—	—
26	609374.66	7625917.71	BG02-11A1	Mylonite	31.12	455.92	600.41	13.83	11.24	—	—	—	—
27	609659.97	7625969.28	BG02-10A1	Protomylonite	31.41	597.24	421.77	11.29	14.66	153.91	154.97	31.29	31.13
28	609805.60	7623656.06	BG04-44B1	Mylonite	31.56	508.93	622.58	12.73	10.94	—	—	—	—
29	610316.74	7620465.17	BG04-53A1A	Protomylonite	32.07	365.89	518.42	16.31	12.55	—	—	—	—
30	610316.74	7620465.17	BG04-53A1B	Protomylonite	32.07	497.68	599.54	12.95	11.25	—	—	—	—
31	610385.54	7622453.58	BG04-50B1	Mylonite	32.14	327.77	578.55	17.72	11.56	—	—	—	—
32	611063.90	7619655.64	BG04-40A1A	Coarse granular	32.82	442.45	993.27	14.14	7.70	—	—	—	—
33	611063.90	7619655.64	BG04-40A1B	Coarse granular	32.82	446.89	1288.52	14.04	6.33	—	—	—	—
34	611843.80	7623342.09	BG04-47A1A	Protomylonite	33.60	493.88	447.23	13.02	14.03	43.3	67.59	81.19	58.09
35	611843.80	7623342.09	BG04-47A1B	Protomylonite	33.60	460.50	416.81	13.72	14.79	43.8	69.65	80.49	56.79
36	612376.68	7619017.43	BG04-38A1A	Protomylonite	34.13	373.27	660.27	16.07	10.47	—	—	—	—

37	612376.68	7619017.43	BG04-38A1B	Protomylonite	34.13	460.50	416.81	13.72	14.79	—	—	—	—
38	615207.58	7620438.46	TH04-1B1	Protomylonite	36.96	627.86	450.68	10.87	13.95	147.88	150.08	32.24	31.89
39	619822.01	7616652.13	TH04-6B1A	Protomylonite	41.57	621.61	471.12	10.953	13.491	131.10	120.93	35.30	37.51
40	619822.01	7616652.13	TH04-6B1B	Protomylonite	41.57	591.30	419.31	11.372	14.726	123.34	109.50	36.95	40.41
41	624393.13	7613121.15	THO4-5A1	Protomylonite	46.14	640.55	495.06	10.70	12.99	149.75	143.13	31.94	33.04

Distance: distance from westernmost sample KA04-6A, projected along an E-W striking transect; d: grain size; ECD: equivalent circular dimeter: LI: linear intercept; σ: differential stress; grain size is reported with its corrected value, using a correction factor of 1.2 and 1.5 for the ECD and LI methods, respectivly.

References

Brey, G.P., and Köhler, T., 1990, Geothermobarometry in four-phase Lherzolites II. New thermobarometers, and practical assessment of existing thermobarometers: Journal of Petrology, v. 31, no. 6, pp. 1353–1378.

Chatzaras, V., Kruckenberg, S.C., Cohen, S.M., Medaris, L.G., Withers, A.C., and Bagley, B., 2016, Axial-type olivine crystallographic preferred orientations: The effect of strain geometry on mantle texture: Journal of Geophysical Research-Solid Earth, v. 121, pp. 4895–4922, doi: 10.1002/2015JB012628.

Lopez-Sanchez, M.A., and Llana-Fúnez, S., 2015, An evaluation of dif- ferent measures of dynamically recrystallized grain size for pa- leopiezometry or paleowattometry studies: Solid Earth, v. 6, no. 2, pp. 475–495, doi: 10.5194/se-6-475-2015.

Taylor, W.R., 1998, An experimental test of some geothermometer and geobarometer formulations for upper mantle peridotites with application to the thermobarometry of fertile lherzolite and garnet websterite: Neues Jahrbuch für Geologie und Paläontologie Abhandlugen, v. 172, no, 2-3, pp. 381–408.

Underwood, E., 1970, Quantitative Stereology, Addison-Wesley, Reading, Mass.

Witt-Eickschen, G., and Seck, H.A., 1991, Solubility of Ca and Al in orthopyroxene from spinel peridotite: an improved version of an empirical geothermometer: Contributions to Mineralogy and Petrology, v. 106, no, 4, pp. 431–439.